

# Vortex-induced vibration of a long flexible cylinder in uniform cross-flow

Chunning Ji<sup>\*1</sup>, Ziteng Peng<sup>1a</sup>, Md. Mahbub Alam<sup>2b</sup>,  
Weilin Chen<sup>1c</sup> and Dong Xu<sup>1d</sup>

<sup>1</sup>State Key Laboratory of Hydraulic Engineering Simulation & Safety,  
Tianjin University, Tianjin, 300072, China

<sup>2</sup>Institute for Turbulence-Noise-Vibration Interaction and Control, Shenzhen Graduate School,  
Harbin Institute of Technology, Shenzhen, 518055, China

(Received September 18, 2017, Revised December 10, 2017, Accepted December 27, 2017)

**Abstract.** Numerical simulations are performed of a long flexible cylinder undergoing vortex-induced vibration at a Reynolds number of 500. The cylinder is pinned at both ends, having an aspect ratio of 100 (cylinder length to cylinder diameter) and a mass ratio of 4.2 (structural mass to displaced fluid mass). Temporal and spatial information on the cross-flow (CF) and in-line (IL) vibrations is extracted. High modal vibrations up to the 6<sup>th</sup> in the CF direction and the 11<sup>th</sup> in the IL direction are observed. Both the CF and IL vibrations feature a multi-mode mixed pattern. Mode competition is observed. The 2<sup>nd</sup> mode with a low frequency dominates the IL vibration and its existence is attributed to a wave group propagating back and forth along the span. Distributions of fluid force coefficients are correlated to those of the CF and IL vibrations along the span. Histograms of the  $x$ - $y$  motion phase difference are evaluated from the total simulation time and a complete vibration cycle representing the standing or travelling wave pattern. Correlations between the phase difference and the vibrations are discussed. Vortex structures behind the cylinder show an interwoven near-wake pattern when the standing wave pattern dominates, but an oblique near-wake pattern when the travelling wave pattern prevails.

**Keywords:** numerical simulation; long flexible cylinder; vortex-induced vibration; mode; fluid force coefficient; phase difference; vortex structure

## 1. Introduction

Vortex-induced vibration (VIV) of marine structures is of practical interest to ocean engineering in the actual application. For example, VIV-induced fatigue damage is one of the most common failures for cylindrical marine structures, such as risers, pipelines, and tendons. Recently, great strides have been achieved in understanding the mechanisms involved in this complicated dynamic process and the comprehensive reviews can be found in Sarpkaya (2004), Williamson and Govardhan (2004, 2008) and Wu *et al.* (2012).

The majority of research efforts on VIV in the past have been focused on the study of rigid cylinders (Jauvtis and Williamson 2004, Assi *et al.* 2013, Bourguet and Jacono 2014, Kim and Alam 2015, Qin *et al.* 2017). There are considerably fewer publications for VIV of slender flexible cylinders. Vandiver (1993) experimentally studied the VIV of a flexible cylinder in uniform cross-flow. An empirical formula was proposed to predict the drag force by using the transverse vibration amplitude of the cylinder. Brika and Laneville (1993) investigated the VIV of a flexible cable.

The first mode of vibration was excited. It was also found that different vortex-shedding patterns occur at 'lock-in', similar to those observed behind rigid cylinders (Williamson and Roshko 1988). The switch between the vibration branches shows hysteresis, corresponding to the phase jump between the displacement and the lift. Huera-Huarte and Bearman (2009a, b) carried out a series of laboratory experiments in which a flexible cylinder was partly submerged in water. Three different tensions were adopted. The initial, upper and lower branches were observed for the smallest tension case. Whereas the lower branch vanished for the other two cases. It was also found that the dual resonance, i.e., the in-line (IL) and cross-flow (CF) vibrations resonate simultaneously, was featured by the 'figure-eight' trajectories, the third harmonic in lift, and the steady IL to CF vibration phase difference. The 2S vortex-shedding pattern, i.e., two single vortices alternately shed in one cycle, was found near the supporting ends while the vortex-shedding pattern in the mid-span of the cylinder switched between 2S and 2P (two vortex pairs alternately shed in one cycle). Similar findings were also reported in Chaplin *et al.* (2005).

Due to the very demanding computational requirements of three-dimensional (3D) computational fluid dynamics (CFD) simulations, the numerical investigation on the VIV of a slender cylinder is rare, especially the one with a large aspect ratio. Newman and Karniadakis (1997) carried out a direct numerical simulation (DNS) of a flexible cylinder in uniform cross-flow. Periodic boundary conditions were applied to simulate the VIV of a slender cylinder with an

\*Corresponding author, Professor

E-mail: [cnji@tju.edu.cn](mailto:cnji@tju.edu.cn)

<sup>a</sup> Graduate Student

<sup>b</sup> Professor

<sup>c</sup> Graduate Student

<sup>d</sup> Associate Professor

infinite length. Two vibration modes, i.e., the standing and travelling wave modes, were found. Because of the low-energy feature of the travelling wave mode, the standing wave vibration finally transformed into the travelling wave one. It was also reported in Newman and Karniadakis (1997) that the near-wake showed an oblique vortex-shedding pattern in the travelling wave vibration, but exhibited an interwoven vortex-shedding pattern in the standing wave vibration. Bourguet *et al.* (2011) numerically investigated the VIV of a flexible cylinder in shear-flow. A combined standing and travelling wave pattern was observed. Lucor *et al.* (2006) studied the distribution and variation of the hydrodynamic forces on a flexible cylinder undergoing VIV in shear-flow. The influences of different flow profiles, i.e., linear and exponential shear flows, were investigated.

In this paper, the VIV of a flexible cylinder in a uniform cross-flow is numerically investigated. The aspect ratio of the cylinder is 100, the Reynolds number and the mass ratio are 500 and 4.2, respectively. The normalized tension is 170. The structural damping is set to zero in order to encourage large-amplitude oscillation of the cylinder.

## 2. Numerical methodology

The governing equations for fluid flow are the incompressible Navier–Stokes equations. The fluid-structure interaction (FSI) is simulated by using the immersed boundary (IB) method which was first introduced by Peskin (1972) in the simulation of blood flow around the flexible leaflet of a human heart. In the framework of the IB method, the flow governing equations are discretized on a fixed Cartesian grid, which generally does not conform to the geometry of moving structures. As a result, the boundary conditions on the fluid-structure interface (which manifest the interaction between fluid and structure) cannot be imposed directly. Instead, an extra body force is added into the momentum equation by using interpolation and distribution functions to take such interaction into account. Compared with conventional FSI numerical methods, the IB method has significant advantages, particularly in the FSI simulations with topological changes.

The conservative form of the second-order Adams-Bashforth temporal-discretized governing equations of incompressible fluid flow using the IB method are

$$\mathbf{u}^{n+1} = \mathbf{u}^n + \delta t \left( \frac{3}{2} \mathbf{h}^n - \frac{1}{2} \mathbf{h}^{n-1} - \frac{3}{2} \nabla p^n + \frac{1}{2} \nabla p^{n-1} \right) + \mathbf{f}^{n+\frac{1}{2}} \delta t \quad (1)$$

$$\nabla \cdot \mathbf{u}^{n+1} = 0 \quad (2)$$

where,  $\mathbf{u}$  is the velocity,  $p$  is the pressure,  $\mathbf{h} = \nabla \cdot (-\mathbf{u}\mathbf{u} + \nu(\nabla\mathbf{u} + \nabla\mathbf{u}^t))$  comprises of the convective and diffusive terms,  $\nabla$  denotes gradient operator, the superscript  $t$  is matrix transposition, and superscript  $n+1$ ,  $n+1/2$ ,  $n$ ,  $n-1$  indicate the time step.  $\mathbf{f}$  denotes the extra body force on the Cartesian grid and is calculated as

$$\mathbf{f}^{n+\frac{1}{2}} \delta t = D(\mathbf{F}^{n+\frac{1}{2}}) = D(\mathbf{V}^{n+1} - I(\mathbf{u}^n + \delta t(\frac{3}{2}\mathbf{h}^n - \frac{1}{2}\mathbf{h}^{n-1} - \frac{3}{2}\nabla p^n + \frac{1}{2}\nabla p^{n-1}))) \quad (3)$$

where,  $\mathbf{F}$  is the extra body force on the IB points,  $\mathbf{V}$  is the desired velocity of the IB points obtained by solving the governing equation of cylinder motion,  $I(\phi, \mathbf{X}_i)$  and  $D(\Phi, \mathbf{x})$  are the interpolation and distribution functions suggested by Peskin (2002), respectively. Note that, the lower-case  $\phi(\mathbf{x})$  represents the variables on the Cartesian grid  $\mathbf{x}$ , such as  $\mathbf{u}$ ,  $p$ ,  $\mathbf{f}$ , etc., while the upper-case  $\Phi(\mathbf{X}_i)$  indicates the variables on the IB points  $\mathbf{X}_i$ , such as  $\mathbf{V}$ ,  $\mathbf{F}$ , etc. The interpolation function projects physical fields from the Cartesian grids to the IB points. On the other hand, the distribution function maps physical fields from the IB points back to the Cartesian grids.

The two-step predictor-corrector procedure is adopted for the decoupling of the flow governing equations (Eqs. (1)-(3)). The resultant pressure Poisson equation is solved by using the bi-conjugate gradient stabilized method – BiCGSTAB (Van der Vorst 1992), preconditioned by using the geometric multi-grid method. For the sake of conciseness, details of the methodology are not presented here. Please refer to our previous work (Ji *et al.* 2012) for further information.

The flexible cylinder is modelled as a pinned-pinned top tension cable on the consideration of the large aspect ratio of a marine riser in reality. The bending stiffness of the cylinder is neglected. The mass ratio is  $m = \rho_c / \rho_f D^2$ , where  $\rho_c$  is the cylinder mass per unit length,  $\rho_f$  is the fluid density, and  $D$  is the cylinder diameter. The normalized tension is  $T = \tau / \rho_f D^2 U_\infty^2$ , where  $\tau$  is the tension, and  $U_\infty$  is the free-stream velocity. The non-dimensional phase velocity in a vacuum is calculated as  $\omega = \sqrt{T/m}$ . The non-dimensional  $i^{\text{th}}$  natural frequency in a vacuum is  $f_{i,v} = \omega / \lambda_i$ , where  $\lambda_i$  is the normalized  $i^{\text{th}}$  wavelength. The non-dimensional governing equation for the structural dynamic can be expressed as follows.

$$m \ddot{\zeta}(x, y) - T \zeta''(x, y) = \frac{C(x, y)}{2} \quad (4)$$

where,  $\zeta(x, y)$  is the displacement normalized by the cylinder diameter,  $C(x, y) = 2F(x, y) / \rho_f D U_\infty^2$  is the hydrodynamic force coefficient,  $F(x, y)$  is the hydrodynamic force. The superscripts  $\cdot\cdot$  and  $''$  represent the second-order time and space derivatives, respectively. The governing equation is discretized by using the 3D 2-node cable element. Each node has three degree of freedoms (DOF). The Newmark- $\beta$  method which is unconditionally stable and second-order accurate is adopted for time marching.

Table 1 Comparison of the VIV of an isolated cylinder in cross-flow

	$Y_{\max}/D$	$C_{d\text{mean}}$	$C_{l\text{max}}$	$St$
Shiels <i>et al.</i> (2001)	0.58	2.22	0.77	0.196
Shen <i>et al.</i> (2009)	0.57	2.15	0.83	0.190
Bourguet and Jacono (2014)	0.57	2.08	0.88	0.188
Present work	0.57	2.09	0.75	0.185

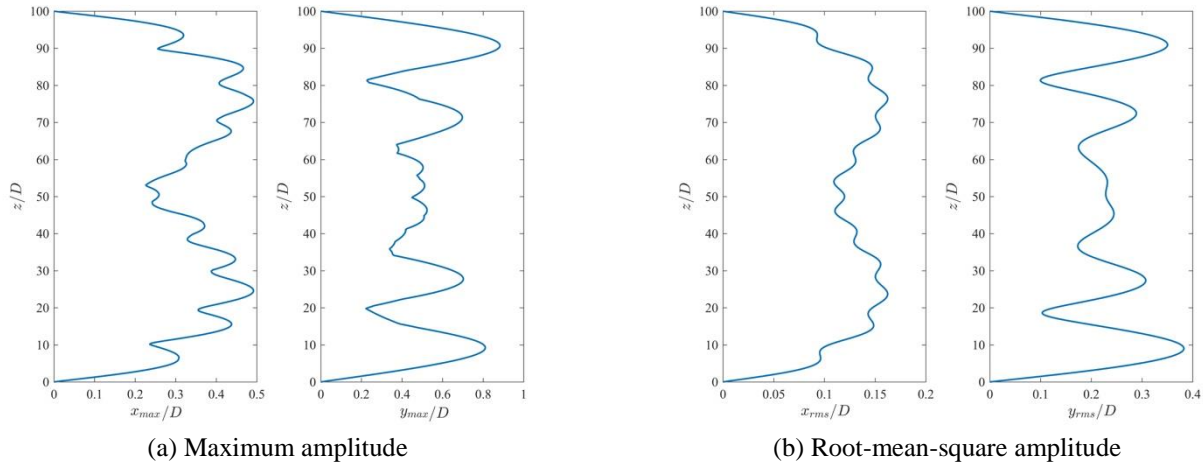


Fig. 1 Distribution of the displacement amplitude along the span

To examine the accuracy of the numerical methodology, the VIV of an isolated cylinder in cross-flow was simulated. The computational domain size is  $200D$  and  $100D$  in the streamwise and transverse directions. A uniform mesh with the non-dimensional grid spacing of  $\Delta x/D = \Delta y/D = 1/64$  is used for discretization. The Reynolds number is  $Re=100$ , the mass ratio is  $m=1.25$ , the reduced velocity is  $U_r = U_\infty / f_n D = 4.46$ ,  $f_n$  is the natural frequency of the vibration system. Table 1 compares the vibration amplitude, hydrodynamic forces and vibration frequency between the present and published results. A good agreement is achieved between the results. More validation cases can be found in Chen *et al.* (2015a, b).

### 3. Results and discussions

#### 3.1 Simulation parameters

The simulation is carried out in a rectangular computational box  $\Omega = [-8D, 32D] \times [-10D, 10D] \times [0, 100D]$  discretized by a Cartesian mesh with a resolution of  $512 \times 192 \times 384$  (streamwise  $\times$  transverse  $\times$  spanwise). The flexible cylinder is initially placed at the origin of the  $X$ - $Y$  plane. In the vicinity of the cylinder (a square region of  $[-2D, 22D] \times [-2D, 2D]$  in the  $X$ - $Y$  plane), a uniform mesh with a grid spacing of  $\Delta x = \Delta y = D/32$  is used.

Beyond that, a stretched mesh is adapted on the consideration of keeping the total number of grids within a reasonable range. Along the cylinder span, totally 385 planes are adopted with a grid spacing of  $\Delta z \approx 0.26D$ . The Dirichlet inflow boundary condition is used together with free-slip side boundary conditions. A Neumann-type boundary condition is adopted at the outflow. The number of IB points for the cylinder is 202 on the  $X$ - $Y$  plane to ensure at least one IB point is allocated in each grid cell. Other simulation parameters are: the Reynolds number  $Re=500$ , the non-dimensional tension is  $T=170$ , the mass ratio  $m=4.2$  and the normalized time step size is  $\Delta t U_\infty / D = 0.0025$ .

#### 3.2 Vibration response

Fig. 1 shows the maximum and root-mean-square (r.m.s.) amplitudes of the displacement in the IL and CF directions, respectively. Note that the time-averaged streamwise displacement is deducted in the calculation of the IL amplitudes. Both IL and CF amplitudes are symmetric about the cylinder's midpoint at  $z/D=50$ . The IL max amplitude,  $x_{\max}$ , shows two major peaks on which eleven minor peaks superimposed while the CF max amplitude,  $y_{\max}$ , demonstrates two major peaks on each side and a flattened and spanwise elongated peak in the middle. Obvious fluctuations can be found on this mid-span

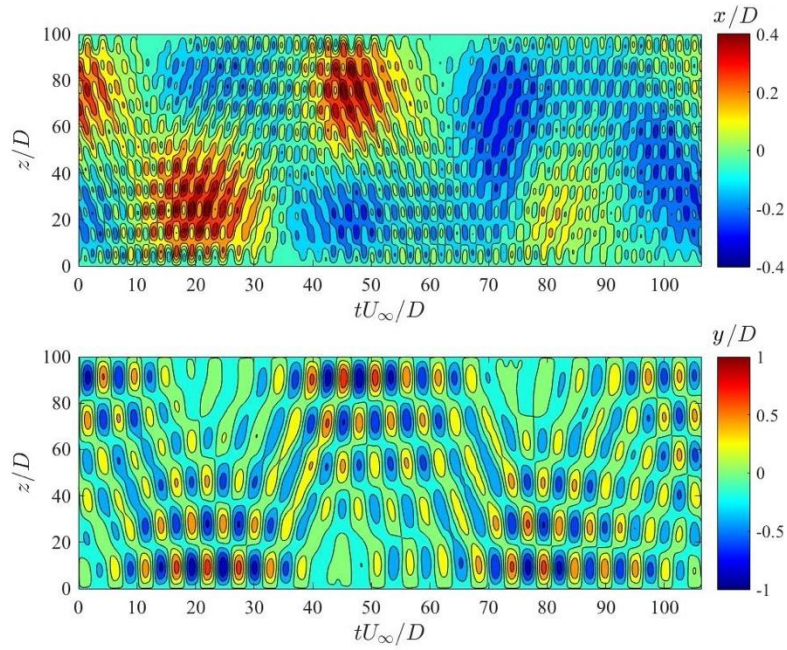


Fig. 2 Time-space distribution of the IL (upper) and CF (lower) displacement

peak. The largest  $x_{max}$  is  $0.49D$  achieved at  $z/D=25$  and  $75$ . It is comparable to the largest  $y_{max}$  of  $0.89D$  obtained at  $z/D=90$ . This is different from the VIV response of an elastically-supported rigid cylinder in which the IL amplitude is one order of magnitude smaller than the CF counterpart. The flattened CF peak in the mid-span implies the presence of the travelling wave pattern in this region while the augmented CF peaks near the ends indicate the prevailing standing wave pattern. Moreover, the peak amplitudes near both ends roughly double the one in the middle, suggesting the perfect reflection of the propagating wave. The IL and CF r.m.s. amplitudes show similar patterns discussed above except that the variation is smoother. The amplitudes are approximately symmetric about the midpoint, and have the maximum values of  $0.16D$  and  $0.38D$  in the IL and CF directions, respectively.

Fig. 2 shows the time-space distribution of the IL and CF displacement. The combined standing and travelling wave pattern is obvious in the CF displacement. For example, in the mid-span, the CF displacement shows the standing wave pattern during  $19.5 < tU_{\infty}/D < 24$  but displays the travelling wave pattern during  $32.5 < tU_{\infty}/D < 40$ . The two patterns alternately dominate the CF vibration. The IL displacement shows a multi-component vibration pattern with a low-frequency dominated component travelling with high-frequency ones. The standing wave pattern is observed at the very ends due to the wave reflection. The above observations are consistent with the spanwise distribution of the IL and CF amplitudes, as shown in Fig. 1.

An interesting phenomenon observed is that a wave group composed of several individual waves propagates

back and forth along the span. Because the structural damping is zero, the amplitude of the wave group is not significantly reduced, despite some fluctuations in the IL displacement. When the wave group is reflected from one end, the displacement shows the standing wave pattern. On the other hand, when the wave group propagates half-way to the other end, the displacement shows the travelling wave pattern in the mid-span.

Fig. 3 shows the distribution of the power spectral density (PSD) of the displacement calculated by using the fast Fourier transform. It can be seen that the IL vibration shows the co-existence of three components, i.e., the 2<sup>nd</sup>, 10<sup>th</sup> and 11<sup>th</sup> mode of vibration. Among these, the 2<sup>nd</sup> mode is predominant while the 10<sup>th</sup> mode is rather weak. The CF vibration consists of the 5<sup>th</sup> and 6<sup>th</sup> mode of vibration, with the former slightly prevalent. The multi-mode vibration is the unique feature of the VIV of a flexible cylinder, especially for the one with a large aspect ratio. A possible reason is related to the IL bending of the cylinder which gives rise to the varying local normal velocity (thus the varying local reduced velocity) along the cylinder. It should be noticed that the 2<sup>nd</sup> mode of vibration in the IL direction is not related to the periodical vortex shedding but is caused by the low-frequency propagating wave group.

The PSD plots of the displacement only show the time-averaged characteristics of the vibration modes. To investigate their temporal evolutions, the time histories of the vibration mode in the IL and CF directions are calculated by applying the mode decomposition method (Huera-Huarte and Bearman 2009a). Obvious mode competition is observed, as seen in Fig. 4. In the CF vibration, the competition is between the 5<sup>th</sup> and 6<sup>th</sup> modes while in the IL vibration, the competition is between the 10<sup>th</sup> and 11<sup>th</sup> modes. The mode competition of the IL

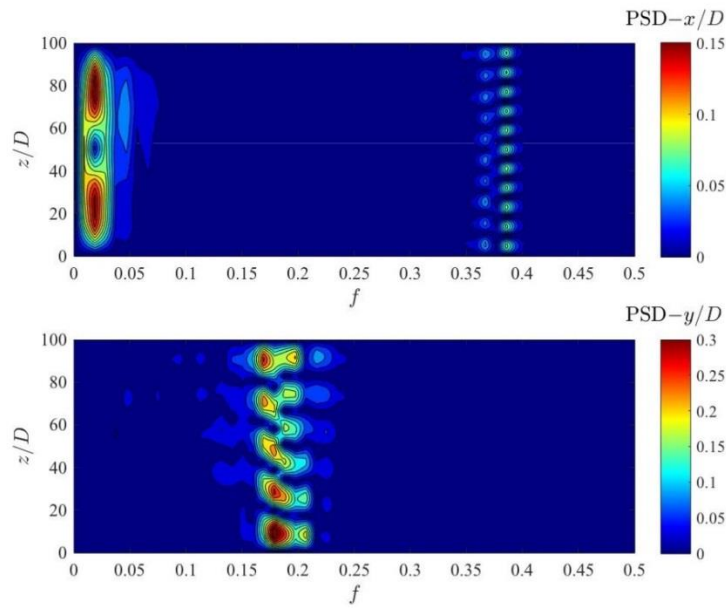


Fig. 3 Power spectral density of the IL and CF displacement

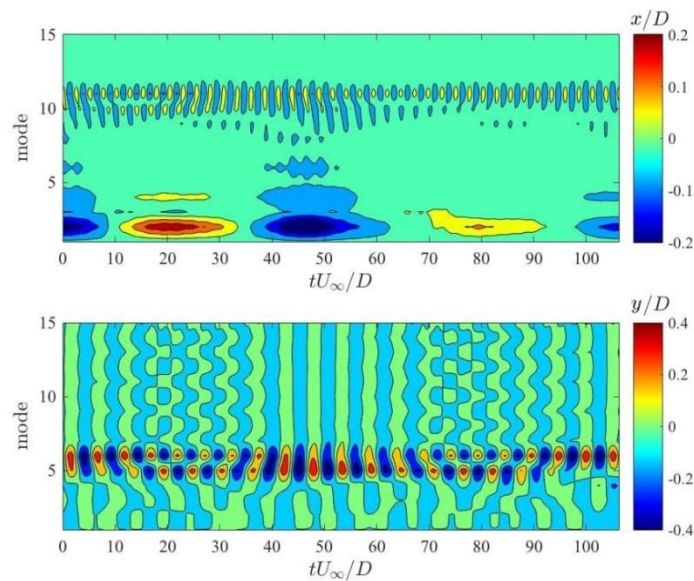


Fig. 4 Time histories of the streamwise and transverse vibration mode

displacement is not well demonstrated due to the existence of the predominant 2<sup>nd</sup> mode. However, by filtering out this low-frequency component, the competition is revealed as will be discussed in Section 3.3. Upon closer inspection on the modal histories, it can be found that when the wave group is reflected from the lower end ( $z/D=0$ ), the CF vibration shows the co-existence of the 5<sup>th</sup> and 6<sup>th</sup> modes. However, when the wave group echoes off the upper end ( $z/D=100$ ), the CF vibration shows a single-mode pattern, either 5<sup>th</sup> or 6<sup>th</sup> mode.

### 3.3 Modal decomposed vibration response

As discussed above, the IL displacement has multiple components and is dominated by the 2<sup>nd</sup> mode of vibration with a rather low frequency. However, this low-frequency vibration component is not connected to vortex-excited vibration due to its significant difference from the vortex-shedding frequency. To clearly show the characteristics of the vortex-induced vibration, in this section and hereafter, the low-frequency component is filtered out, and the retained high-frequency vibration is investigated. The

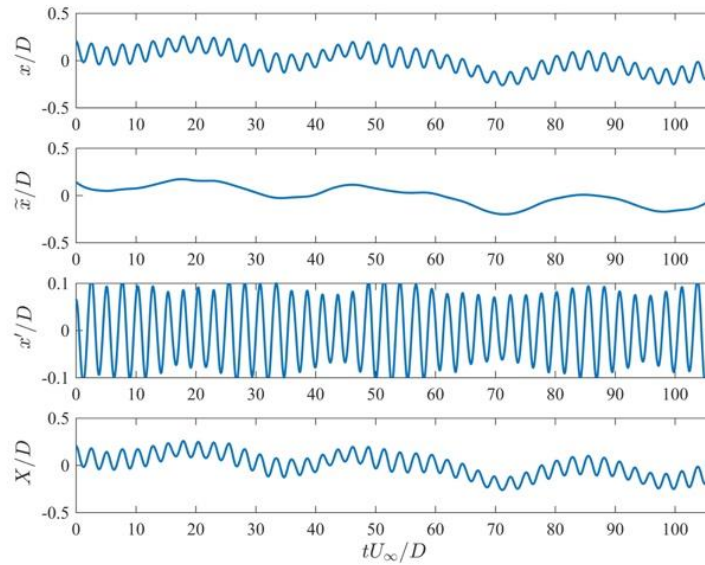


Fig. 5 Mode decomposition of the IL displacement at the mid-span point.  $x$  is the original signal,  $\tilde{x}$  is the low-frequency component,  $x'$  is the retained high-frequency component,  $X$  is the reconstructed signal

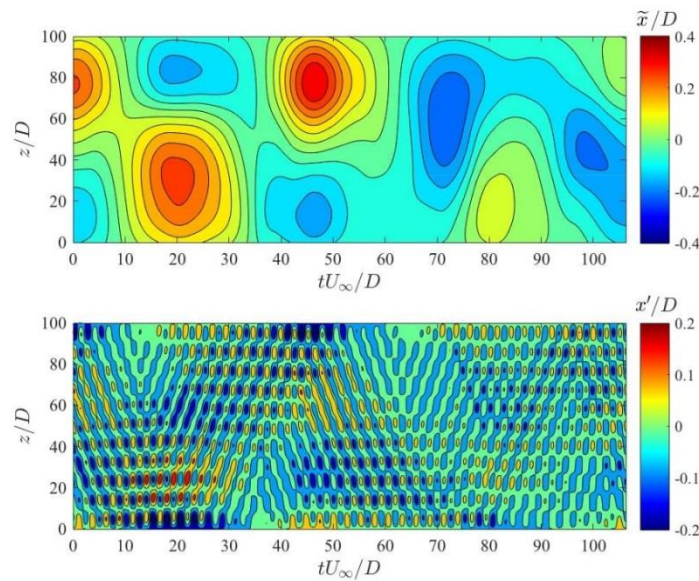


Fig. 6 Time-space distribution of the low-frequency (upper) and high-frequency (lower) components of the IL displacement

purpose of this treatment is to purify the ‘contaminated’ results by the 2<sup>nd</sup> mode of vibration and thus the vibration characteristics are more meaningful in physics.

Fig. 5 shows the decomposition of the IL displacement at the mid-span point. The low-frequency component  $\tilde{x}$  is identified by using the multilevel wavelet decomposition function, i.e. `wavedec2`, in Matlab and removed from the original signal  $x$ . `Wavedec2` returns the wavelet decomposition of a two-dimensional matrix, i.e., the time-space variation of vibration responses, using a wavelet named ‘`sym7`’ in this study. The retained vibration response

still contains multiple components as indicated by the varying amplitude of  $x'$ . To check the accuracy of the decomposition, Fig. 5 also shows the reconstructed signal  $X$  which is virtually equivalent to the original one.

Fig. 6 shows the temporal and spatial evolution of the decomposed low-frequency vibration  $\tilde{x}$  and the remained  $x'$ . For  $tU_\infty/D < 60$ ,  $\tilde{x}$  shows the 2<sup>nd</sup> mode of vibration with a maximum amplitude roughly  $0.4D$ . However, it incorporates the 1<sup>st</sup> mode of vibration when  $tU_\infty/D > 60$

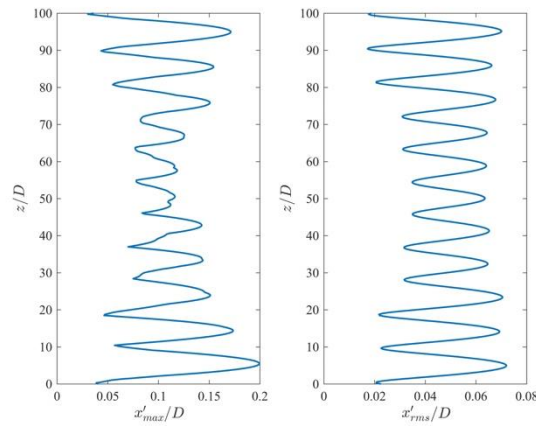


Fig. 7 Distribution of the maximum and root-mean-square amplitudes of the IL displacement along the span

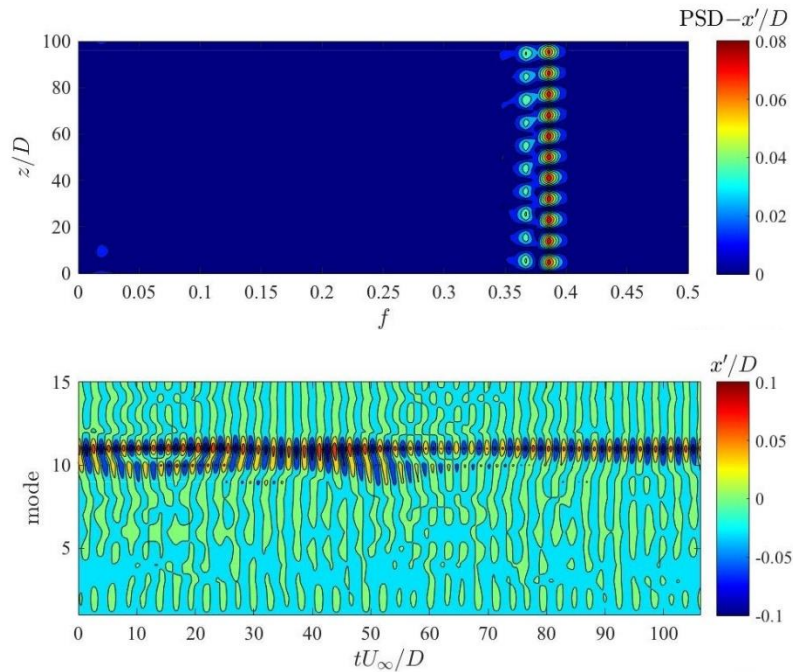


Fig. 8 Power spectral density (upper) and vibration mode history (lower) of the high-frequency component of the IL displacement

despite the amplitude is reduced. The  $x'$  shows a pattern similar to that of the CF displacement in Fig. 2. Standing wave pattern dominates near the two ends of the cylinder while the travelling and standing wave patterns alternately appear in the mid-span with the former prevalent. The back and forth propagation of a wave group is observed again in  $x'$ . However, upon closer inspection, it can be seen that the IL wave group is slightly ahead, about one-tenth of the 2<sup>nd</sup> modal period, of its CF counterpart.

Fig. 7 shows the max and r.m.s. amplitudes of  $x'$ . Both display larger peaks near the ends and smaller ones in the middle, although this trend is less prominent in the r.m.s. amplitude. This is similar to the variation of  $y_{max}$  along the span and can be attributed to the wave reflection at the

ends. Compared to the amplitudes of the original displacement  $x$ , the two major peaks disappear and the eleven minor peaks are thus more protruding. The maxima of the max and r.m.s. amplitudes are  $0.2D$  and  $0.07D$ , respectively, which are substantially smaller than the CF counterparts. From this point of view, the IL vibration amplitude (vortex-induced) is roughly one order of magnitude smaller than that in the CF direction, which agrees with the observations in the VIV of an elastically-mounted rigid cylinder.

Fig. 8 shows the frequency spectra and the mode decomposition of  $x'$ . The competition between the 10<sup>th</sup> and 11<sup>th</sup> modes of vibration is clearly demonstrated.

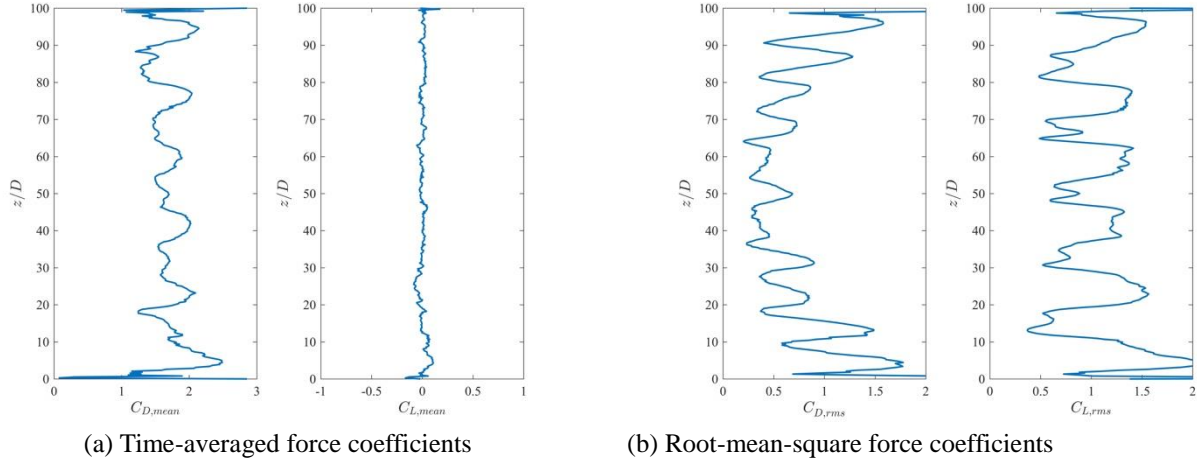


Fig. 9 Distribution of the time-averaged and root-mean-square force coefficients.

### 3.4 Hydrodynamic forces

Fig. 9 shows the spanwise distributions of the time-averaged and r.m.s. force coefficients. It is seen that  $C_{D,mean}$  shows six peaks along the span similar to the CF vibration amplitude. However,  $C_{D,rms}$  shows a distribution with eleven peaks, although the two peaks adjacent to the mid-span peak are less protruding, which is analogous to the IL vibration amplitude. This difference can be explained as follows. The  $C_{D,mean}$  is closely correlated with the time-averaged pressure difference around the cylinder. At the antinodes of the CF displacement, the time-averaged pressure behind the cylinder is lower than that at the CF vibration nodes due to the larger CF amplitude. This causes a larger drag at the CF vibration antinodes. However,  $C_{D,rms}$  is linked with the instantaneous IL vibration and the local vortex-shedding, and thus shows the same variation with that of the IL amplitude. In the mid-span,  $C_{D,rms}$  is obviously smaller than that near the ends. This can be attributed to the local smaller IL vibration amplitude. As expected, the mean lift coefficient  $C_{L,mean}$  is close to zero with small fluctuations. The r.m.s. lift coefficient,  $C_{L,rms}$ , behaves similarly to the CF vibration amplitude along the span, see Fig. 9 (b).

### 3.5 Phase difference of $x'$ - $y$ motion

According to the suggestion of Bourguet *et al.* (2011), the phase difference between the IL and CF displacements is defined as

$$\phi_{x'y} = [\phi_x - \phi_y, \text{mod } 360^\circ] \quad (5)$$

where,  $p$  and  $q$  are two integer numbers defining the level of synchronization. In this paper,  $p = 1$  and  $q = 2$  are adopted considering the dominant frequencies of  $x'$  and  $y$  as shown in Figs. 3 and 8. Note that the vibration response

corresponding to the 2<sup>nd</sup> mode of IL vibration is excluded because it is caused by the travelling wave group. As stated in Bourguet *et al.* (2011), when  $0^\circ < \phi_{x'y} < 180^\circ$ , the trajectory of the cylinder motion is counter-clockwise, i.e., the cylinder moves upstream when approaching the CF vibration maxima. On the contrary, when  $180^\circ < \phi_{x'y} < 360^\circ$ , the trajectory is clockwise. The switches between the counter-clockwise and the clockwise orbits usually match the nodes and anti-nodes of vibration. Bourguet *et al.* (2011) stated that when  $0^\circ < \phi_{x'y} < 180^\circ$ , energy-transfer is from fluid flow to structure vibration, and thus the large-amplitude vibrations are excited. However, when  $180^\circ < \phi_{x'y} < 360^\circ$ , energy-transfer is reversed and the vibrations are damped out. However, Vandiver *et al.* (2009) affirmed that  $315^\circ < \phi_{x'y} < 90^\circ$  is favorable to large-amplitude VIV as the motion of the cylinder at the peaks in the CF vibration is opposed to the flow. Conversely,  $135^\circ < \phi_{x'y} < 270^\circ$  is unfavorable to significant VIV.

Fig. 10(a) depicts the histograms of  $\phi_{x'y}$  evaluated from the whole time. It is seen that the distribution of  $\phi_{x'y}$  shows a staggered pattern along the span, concentrating on either  $20^\circ$  or  $220^\circ$  at different sections. This pattern exhibits a connection with the variation of the IL and CF vibration amplitudes. From the ends to the mid-span, the odd IL peaks match the zones with  $\phi_{x'y} = 20^\circ$  while the even IL peaks agree with the zones with  $\phi_{x'y} = 220^\circ$ . Similarly, from the ends to the mid-span, the ascent sections of the CF amplitude curve correspond to  $\phi_{x'y} = 20^\circ$  while the descent sections are linked with  $\phi_{x'y} = 220^\circ$ . This alternating favorable and unfavorable VIV zone pattern is highly coincident with the findings in Vandiver *et al.* (2009). It can also be observed that the transition from the counter-clockwise to the clockwise trajectory links with the anti-

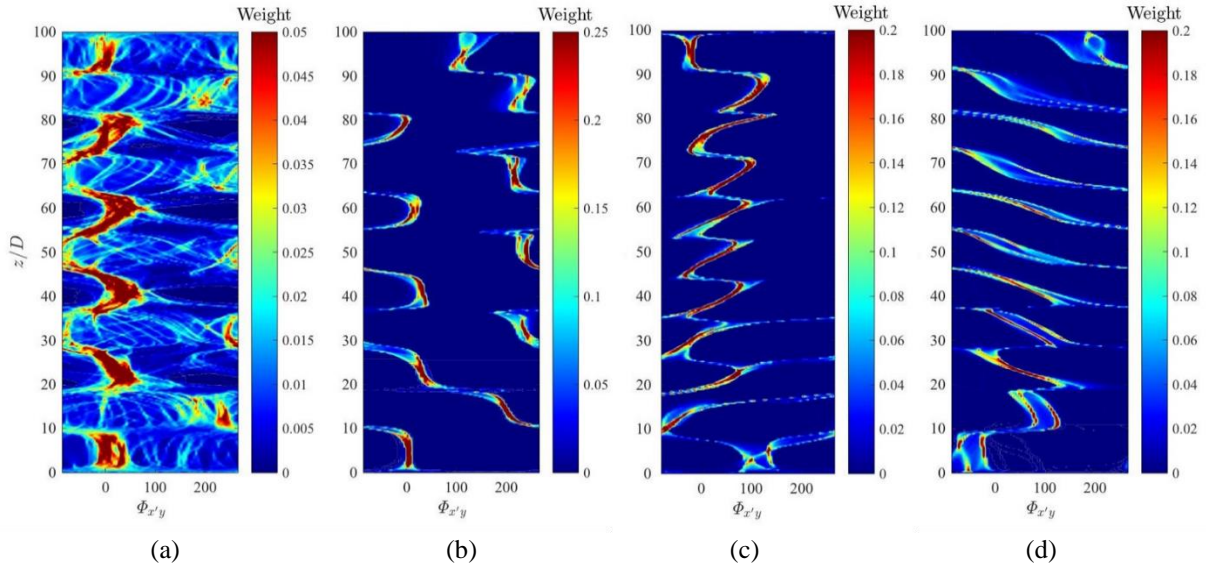


Fig. 10 Histograms of the phase difference between the IL and the CF vibrations. (a): the whole time, (b): the standing wave pattern ( $52.5 < tU_\infty / D < 57.5$ ), (c): the travelling wave pattern (ascending) ( $34 < tU_\infty / D < 40$ ) and (d): the travelling wave pattern (descending) ( $64 < tU_\infty / D < 70$ ).

nodes of the CF vibration while the change from the clockwise to the counter-clockwise orbit relates with the nodes of the CF vibration.

Figs. 10 (b)-10(d) present the histograms of  $\phi_{x'y}$  from a complete vibration cycle representing the standing ( $52.5 < tU_\infty / D < 57.5$ ) and travelling ( $34 < tU_\infty / D < 40$  and  $64 < tU_\infty / D < 70$ ) wave patterns, respectively. In the standing wave pattern,  $\phi_{x'y}$  shows a similar pattern to that discussed above, although the histograms is much purer and the zones are narrower. Between the zones,  $\phi_{x'y}$  displays sharp transitions. However, the distribution of  $\phi_{x'y}$  in the traveling wave pattern is distinct. It shows a continuous variation with in the zones, i.e., increasing along the wave propagation direction (ascending within  $34 < tU_\infty / D < 40$  and descending within  $64 < tU_\infty / D < 70$ ), which implies that the mid-span is dominated by the travelling wave vibration without obvious nodes and anti-nodes. However,  $\phi_{x'y}$  displays phase jumps of  $360^\circ$  between the zones. It is also noticed that  $\phi_{x'y}$  shows invariant sections near the upper ( $34 < tU_\infty / D < 40$ ) and lower ( $64 < tU_\infty / D < 70$ ) ends, indicating the local standing wave vibration caused by the wave reflection. Comparing Figs. 10(a), 10(c) and 10(d), it can be found that the interlaced structures in Fig. 10(a) are actually the superimposed ‘footprints’ of the phase difference in traveling wave pattern. The varying phase difference along the cylinder span can be attributed to the different phase velocities of the CF and IL vibrations in the traveling wave pattern. As discussed in Vandiver *et al.* (2009), the phase velocity of a slender cylinder is dictated

by the bending stiffness and the added mass. In this study, the cylinder is modeled as a tension dominated cable. Its non-dimensional phase velocity in a vacuum is  $\omega = \sqrt{T/m}$  which is frequency independent. As a result, the IL and CF phase velocity should be exactly the same, even if the IL frequency is twice of the CF one as in this study. However, in fluid, the added mass  $m_a$  of a vibrating cylinder can significantly alter the non-dimensional phase velocity  $\omega' = \sqrt{T/(m+m_a)}$ , especially when the mass ratio is small. Considering that the IL and CF vibrations are distinct in both amplitude and frequency, the added mass, and thus the non-dimensional phase velocity, is different in the IL and CF vibrations. Consequently, the phase difference is variant along the cylinder span, as shown in Figs. 10(c) and 10(d).

### 3.6 Near-wake pattern

Fig. 11 shows the vortex-shedding patterns in the near-wake at two time instants. The vortices are visualized by using the iso-surfaces of  $\lambda_2 = -5$  – the second eigenvalue of the symmetric tensor  $\mathbf{S}^2 + \mathbf{\Omega}^2$ , where  $\mathbf{S}$  and  $\mathbf{\Omega}$  are respectively the symmetric and asymmetric parts of the velocity gradient tensor  $\nabla \mathbf{u}$ . The color on the iso-surfaces indicates of the vorticity in the spanwise direction. Fig. 11(a) shows the vortex-shedding pattern at  $tU_\infty / D = 55$  corresponding to the standing wave pattern. It is observed that the spanwise vortex structures are generally parallel to the cylinder indicating the prevalence of the interwoven vortex-shedding pattern. This is different from the vortex-shedding pattern at  $tU_\infty / D = 66$  as shown in Fig. 11(b).

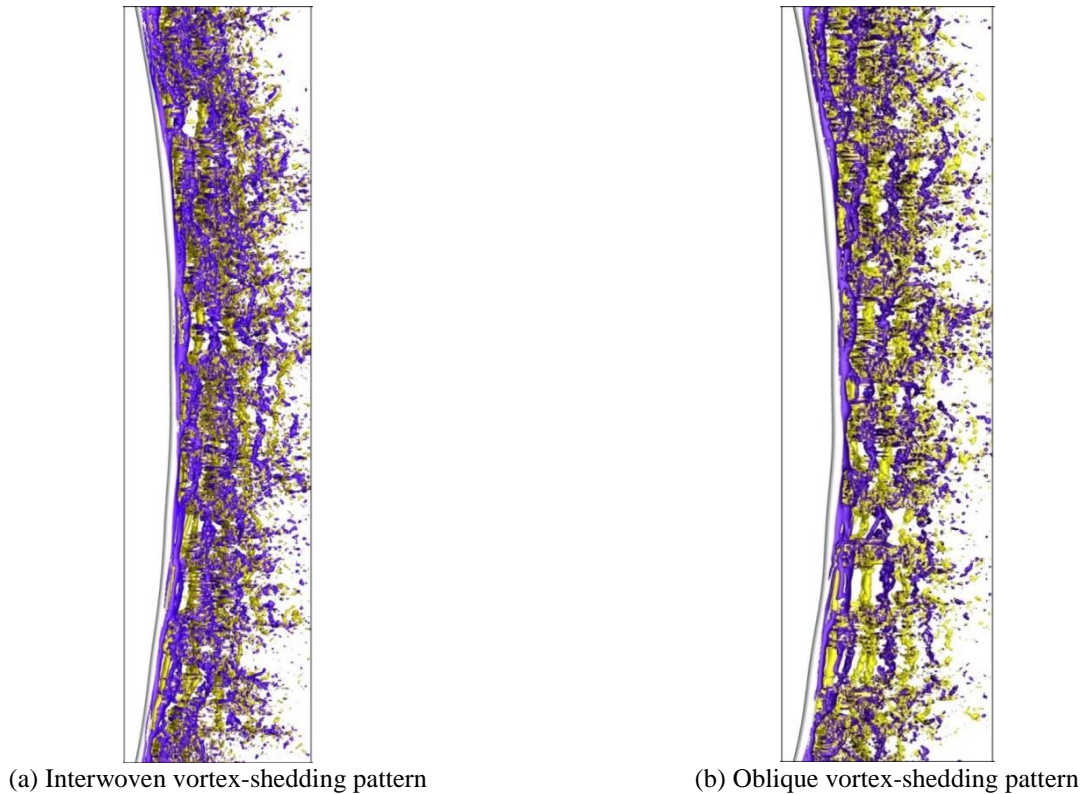


Fig. 11 The vortex-shedding patterns in the near-wake

At  $tU_\infty/D = 66$ , the separated vortex structures are oblique to the cylinder due to the predominant travelling wave vibration. The vortex shedding is phase locked to the traveling wave and create large lifts moving with wave crests. Note that the vortex structures change their oblique directions if the propagation of the traveling wave flips over (not shown here).

#### 4. Conclusions

A numerical investigation is carried out on the vortex-induced vibration of an isolated cylinder in cross-flow at a Reynolds number of 500. The immersed boundary method is applied to solve the interaction between the fluid and the flexible cylinder. The structural dynamics is simulated by using a 3D 2-node cable model. The slender cylinder, with an aspect ratio of 100, is top tensioned and pin-pin supported. The normalized tension is 170, and the mass ratio is 4.2. The investigation leads to the following conclusions.

- (1) The IL and CF displacements show the co-existence of multiple components. Mode competitions between the 10<sup>th</sup> and 11<sup>th</sup> modes (IL) and between the 5<sup>th</sup> and 6<sup>th</sup> mode (CF) are observed.
- (2) The standing and travelling wave patterns alternately dominate the IL and CF vibrations.
- (3) The 2<sup>nd</sup> mode with a very low vibration frequency dominates the IL vibration and its existence is attributed

to the wave group propagating back and forth along the span.

- (4)  $C_{D,mean}$  and  $C_{L,rms}$  show a variation similar to that of the CF displacement while  $C_{D,rms}$  displays a distribution matching the IL displacement.
- (5) Histograms of the  $x$ - $y$  motion phase difference are evaluated from a complete vibration cycle representing the standing or travelling wave pattern. In the standing wave dominated vibration, the sharp transition from the counter-clockwise to the clockwise orbit is connected with the CF vibration anti-node while that from the clockwise to the counter-clockwise trajectory is associated with the CF vibration node. The variation of the phase difference is smooth in the travelling wave governed vibration without sharp transitions.
- (6) Vortex structures behind the cylinder show the interwoven near-wake pattern when the standing wave pattern dominates, but the oblique near-wake pattern when the travelling wave pattern prevails.

#### Acknowledgments

The research described in this paper was financially supported by the Science Fund for Creative Research Groups of the National Natural Science Foundation of China (Grant No. 51621092), National Natural Science Foundation of China (Grant No. 51579175, 51779172), Tianjin Research Program of Application Foundation and Advanced Technology (Grant No. 12JCQNJC02600),

Special Program for Applied Research on Super Computation of the NSFC-Guangdong Joint Fund (the second phase) (Grant No.U1501501).

## References

- Assi, G.R.S., Bearman, P.W., Carmo, B., Meneghini, J., Sherwin, S. and Willden, R. (2013), "The role of wake stiffness on the wake-induced vibration of the downstream cylinder of a tandem pair", *J. Fluid Mech.*, **718**, 210-245.
- Bourguet, R., Karniadakis, G.E. and Triantafyllou, M.S. (2011), "Vortex-induced vibrations of a long flexible cylinder in shear flow", *J. Fluid Mech.*, **677**, 342-382.
- Bourguet, R. and Jacono, D. (2014), "Flow-induced vibrations of a rotating cylinder", *J. Fluid Mech.*, **740**, 342-380.
- Brika, D. and Laneville, A. (1993), "Vortex-induced vibrations of a long flexible circular cylinder", *J. Fluid Mech.*, **250**, 481-508.
- Chaplin, J.R., Bearman, P.W., Huera-Huarte, F.J. and Pattenden, R.J. (2005), "Laboratory measurements of vortex-induced vibrations of a vertical tension riser in a stepped current", *J. Fluid. Struct.*, **21**(1), 3-24.
- Chen, W., Ji, C., Xu, W., Liu, S. and Campbell, J. (2015a), "Response and wake patterns of two side-by-side elastically supported circular cylinders in uniform laminar cross-flow", *J. Fluid. Struct.*, **55**, 218-236.
- Chen, W., Ji, C., Wang, R., Xu, D. and Campbell, J. (2015a), "Flow-induced vibrations of two side-by-side circular cylinders: Asymmetric vibration, symmetry hysteresis and near-wake patterns", *Ocean Eng.*, **110**, 244-257.
- Huera-Huarte, F.J. and Bearman, P.W. (2009a), "Wake structures and vortex-induced vibrations of a long flexible cylinder - part 1: Dynamic response", *J. Fluid. Struct.*, **25**(6), 969-990.
- Huera-Huarte, F.J. and Bearman, P.W. (2009b), "Wake structures and vortex-induced vibrations of a long flexible cylinder - part 2: Drag coefficients and vortex modes", *J. Fluid. Struct.*, **25**(6), 991-1006.
- Jauvtis, N. and Williamson, C.H.K. (2004), "The effect of two degrees of freedom on vortex-induced vibration at low mass and damping", *J. Fluid Mech.*, **509**, 23-62.
- Ji, C., Munjiza, A. and Williams, J.J.R. (2012), "A novel iterative direct-forcing immersed boundary method and its finite volume applications", *J. Comput. Phys.*, **231**(4), 1797-1821.
- Kim, S. and Alam, M.M. (2015), "Characteristics and suppression of flow-induced vibrations of two side-by-side circular cylinders", *J. Fluid. Struct.*, **54**, 629-642.
- Lucor, D., Mukundan, H. and Triantafyllou, M.S. (2006), "Riser modal identification in CFD and full-scale experiments", *J. Fluid. Struct.*, **22**, 905-917.
- Newman, D.J. and Karniadakis, G.E. (1997), "A direct numerical simulation study of flow past a freely vibrating cable", *J. Fluid Mech.*, **344**, 95-136.
- Peskin, C.S. (1972), "Flow patterns around heart valves: A numerical method", *J. Comput. Phys.*, **10**(2), 252-271.
- Peskin, C.S. (2002), "The immersed boundary method", *Acta Numerica*, **11**, 479-517.
- Qin, B., Alam, M.M. and Zhou, Y. (2017), "Two tandem cylinders of different diameters in crossflow: flow-induced vibration", *J. Fluid Mech.*, **829**, 629-658.
- Sarpkaya, T., (2004), "A critical review of the intrinsic nature of vortex-induced vibrations", *J. Fluid. Struct.*, **19**, 389-447.
- Shen, L., Chan, E-S. and Lin, P. (2009), "Calculation of hydrodynamic forces acting on a submerged moving object using immersed boundary method", *Comput. Fluids*, **38**, 691-702.
- Shiels, D., Leonard, A. and Roshko, A. (2001), "Flow-induced vibration of a circular cylinder at limiting structural parameters", *J. Fluid. Struct.*, **15**, 3-21.
- Vandiver, J.K. (1993), "Dimensionless parameters important to the prediction of vortex-induced vibration of long, flexible cylinders in ocean currents", *J. Fluid. Struct.*, **7**(5), 423-455.
- Vandiver, J.K., Jaiswal, V. and Jhingran, V. (2009), "Insights on vortex-induced, traveling waves on long risers", *J. Fluid. Struct.*, **25**(4), 641-653.
- Van der Vorst, H.A. (1992), "Bi-CGSTAB: A fast and smoothly converging variant of Bi-CG for the solution of nonsymmetric linear systems", *SIAM J. Sci. and Stat. Comput.*, **13**(2), 631-644.
- Williamson, C.H.K. and Roshko, A. (1988), "Vortex formation in the wake of an oscillating cylinder", *J. Fluid. Struct.*, **2**(4), 355-381.
- Williamson, C.H.K. and Govardhan, R. (2004), "Vortex-induced vibrations", *Annu. Rev. Fluid Mech.*, **36**, 413-455.
- Williamson, C.H.K. and Govardhan, R. (2008), "A brief review of recent results in vortex-induced vibrations", *J. Wind Eng. Ind. Aerod.*, **96**, 713-735.
- Wu, X.D., Ge, F. and Hong, Y.S. (2012), "A review of recent studies on vortex-induced vibrations of long slender cylinders", *J. Fluid. Struct.*, **28**, 292-308.